Edinburgh Research Explorer

The Simulation of Magnetic Resonance Elastography through Atherosclerosis

The Simulation of Magnetic Resonance Elastography through Atherosclerosis

L. E. J. Thomas-Seale[1*], L. Hollis[1], D. Klatt[2], I. Sack[2], N. Roberts[3], P. Pankaj[4] and P. R. Hoskins[1]

[1]*Centre for Cardiovascular Science, University of Edinburgh, Queen's Medical Research Institute, 47 Little France Crescent, Edinburgh, UK.*

[2]*Department of Radiology, Charité - Universitätsmedizin Berlin, Berlin, Germany*

[3]*Clinical Research Imaging Centre, University of Edinburgh, 47 Little France Crescent, Edinburgh, UK.*

[4]*School of Engineering, University of Edinburgh, Alexander Graham Bell Building, The King's Buildings, Edinburgh, UK.*

* Corresponding Author

Address: Department of Mechanical Engineering, School of Engineering, University of Birmingham, Edgbaston, Birmingham, B15 2TT

Email: Email: l.e.j.thomas-seale@bham.ac.uk / lauren.ej.thomas.seale@gmail.com

Phone: (+44) 0121 4143622 / (+44) 07841 515310

21 **Abstract**

22 The clinical diagnosis of atherosclerosis via the measurement of stenosis size is widely

23 acknowledged as an imperfect criterion. The vulnerability of an atherosclerotic plaque to

24 rupture is associated with its mechanical properties. The potential to image these mechanical

25 properties using magnetic resonance elastography (MRE) was investigated through synthetic

26 datasets.

27 An image of the steady state wave propagation, equivalent to the first harmonic, can be

28 extracted directly from finite element analysis. Inversion of this displacement data yields a

29 map of the shear modulus, known as an elastogram. The variation of plaque composition,

30 stenosis size, Gaussian noise, filter thresholds and excitation frequency were explored.

31 A decreasing mean shear modulus with an increasing lipid composition was identified

32 through all stenosis sizes. However the inversion algorithm showed sensitivity to parameter

33 variation leading to artefacts which disrupted both the elastograms and quantitative trends. As

34 noise was increased up to a realistic level, the contrast was maintained between the fully

35 fibrous and lipid plaques but lost between the interim compositions. Although incorporating a

36 Butterworth filter improved the performance of the algorithm, restrictive filter thresholds

37 resulted in a reduction of the sensitivity of the algorithm to composition and noise variation.

38 Increasing the excitation frequency improved the techniques ability to image the magnitude

39 of the shear modulus and identify a contrast between compositions.

40 In conclusion, whilst the technique has the potential to image the shear modulus of

41 atherosclerotic plaques, future research will require the integration of a heterogeneous

42 inversion algorithm.

43

1. Introduction

Cardiovascular diseases (CVD) were responsible for 31% of global mortalities in 2011 (Mendis et al., 2011). The root cause of the majority these deaths was atherosclerosis (Go et al., 2014). The pathogenesis of atherosclerosis is complex. The primary manifestation of atherosclerosis is an accumulation of lipid in the vascular wall caused by endothelial dysfunction (VanEpps and Vorp, 2007). However factors such as inflammation and biomechanics play a crucial role in the development of the disease (Libby et al., 2002). The rupture of a plaque may be associated with severe clinical events such as heart attack and stroke. The severity of an atherosclerotic plaque and the decision to refer the patient for surgery is based upon symptoms of ischemia and a measurement of the reduction in lumen diameter, known as a stenosis (Packard and Libby, 2008).

The outcome of surgical intervention via carotid endarterectomy, underwent analysis in the North American Symptomatic Carotid Endarterectomy Trial (NASCET) and European Carotid Surgery Trial (ECST). Rothwell et al. (2003) pooled this data and found an 18.7% absolute risk reduction, 5 years post-surgery, for stenoses between 70% and 99%. This statistic demonstrates that approximately 5 endarterectomies are required to prevent the death or stroke of 1 patient. The economic burden of CVD is estimated to be $315 billion in the USA and £19 billion in the UK (Townsend et al., 2012; Go et al., 2014).

A plaques vulnerability to rupture is associated with a number of factors including the size and consistency of the lipid pool, the thickness and mechanical properties of the fibrous cap, inflammation and fatigue in the fibrous cap (Falk et al., 1995). Research is focussed on more definitive diagnostic techniques including, imaging of the plaque composition (Corti and Fuster, 2011), molecular imaging (Mulder et al., 2014), imaging the tissue stiffness (De Korte et al., 2011) and imaging plaque stresses, known as patient specific modelling (Hoskins and Hardman, 2009).

69   Elastography is the overarching term given to elasticity imaging, using a combination of

70   techniques to mechanically excite the tissue and modalities to image the response (Sarvazyan

71   et al., 2011). An inversion algorithm is required to invert an image of displacement into an

72   elastogram of the mechanical properties. Magnetic resonance elastography images the

73   propagation of harmonic, low frequency, mechanical shear waves (Muthupillai et al., 1995).

74   Arterial wall stiffness has been extracted using the Moens-Korteweg equation (Woodrum et

75   al., 2006) and been applied to ex-vivo porcine aortas (Woodrum et al., 2009; Xu et al., 2012)

76   and in-vivo abdominal aortas (Xu et al., 2013). The phase gradient inversion has identified

77   changes in hypertensive aortic stiffness (Kolipaka et al., 2012). The local frequency

78   estimation inversion has measured the relationship between aortic stiffness and age

79   (Damughatla et al., 2015; Kenyhercz et al., 2015). The regional changes in shear modulus

80   through ex-vivo porcine aortas have been measured by Zhang et al. (2016). Other studies

81   have utilised interference elastography to visualise waves in the femoral artery (Zheng et al.,

82   2007) and Fourier decomposed wave reflections to assess stenosis sizes in arterial phantoms

83   (Woodrum et al., 2006).

84   The use of finite element analysis (FEA) is common across the modalities of elastography. It

85   is primarily used as a method of inversion and a selection of studies have used FEA to invert

86   strain images through atherosclerosis (Franquet et al., 2013; Bertoglio et al., 2014). FEA has

87   also been used to create synthetic data sets to assess inversion algorithms (Van Houten et al.,

88   2001; Miller et al., 2015) and explore the sensitivity of technique parameters (Chen et al.,

89   2005). Baldewsing et al. (2004) and Doherty et al. (2013) assessed the application of

90   ultrasound elastography to atherosclerosis by varying the geometric and mechanical

91   properties within finite element models.

92   Measuring arterial stiffness is well established (Parker, 2009), however the term 'stiffness' is

93   used as an overarching term for arterial characteristics that change with response to age or

94 disease (Hamilton et al., 2007). Imaging the specific mechanical properties of arteries is far

95 less wide-spread, the literature contains conflicting results (Barrett et al., 2009) and

96 vasculature-specific experimental data is required (Holzapfel et al., 2014). The parameters of

97 constitutive models for arterial tissue can be extracted using mechanical testing (Holzapfel et

98 al., 2000; Holzapfel et al., 2005). The documentation of the viscoelastic properties of healthy

99 and diseased human arterial tissue is extremely limited. The well cited studies by Loree et al.

100 (1994) and Lee et al. (1991) document the dynamic analysis and viscoelastic properties from

101 ex-vivo samples of the lipid pool and fibrous cap. Viscoelastic properties have been extracted

102 from in-vivo pressure displacement data by Valdez-Jasso et al. (2011). In recent years

103 ultrasound elastography has shown promising results in quantifying the mechanical properties

104 of atherosclerotic plaques (De Korte et al., 2011).

105 A preliminary computational investigation into the variation of the MRE steady state shear

106 wave response through atherosclerotic plaques was undertaken by Thomas-Seale et al.

107 (2011). The aim of this paper is to investigate the potential for MRE to image the shear

108 modulus of atherosclerotic plaques through synthetic datasets.

109 **2. Method**

110 **2.1 Finite Element Analysis**

111 A direct solution, steady state FEA (Abaqus/CAE, Dassault Systèmes Simulia Corp.,

112 Providence, Rhode Island, USA) was applied to allow extraction of a complex wave image,

113 analogous to the first harmonic of Fourier transformed experimental phase images.

114 The 3D geometry (Rhinoceros, McNeel, Seattle, Washington, USA) is displayed in Fig. 1 and

115 Table 1. A plaque and vessel wall was embedded in a block of homogeneous tissue to

116 replicate the transmission of shear waves in-vivo. The global axes and nomenclature are

117 depicted in Fig. 1a and 1b. The region of interest (ROI) is defined as the atherosclerotic

118 plaque.

119 The dimensions of the plaque were based upon a cosine function (Eq. 1), the severity of the

120 stenosis (Eq. 2) and 100% eccentricity (Eq. 3) (Ahmed and Giddens, 1983; Tang et al., 2004).

121 The nomenclature is displayed in Fig. 1 and defined as follows; radius R_0, healthy lumen

122 diameter ϕ_0, stenosis S and the diameter of the narrowest section ϕ_s. At a distance z along

123 the vessel, where z_1 and z_2 are both ends of the stenosis and $R(z)$ is the radius of the vessel.

124 The eccentricity is defined as E_c and e is the distance between the centre point of the vessel

125 and lumen.

$$R(z) = R_0 - SR_0 \left\{ 1 - \cos\left[2\pi \left(z - z_1 \right) / \left(z_2 - z_1 \right) \right] \right\} / 2 \tag{1}$$

$$S = \left(\phi_0 - \phi_s \right) / \phi_0 \times 100\% \tag{2}$$

$$E_c = e / \left[\left(\phi_0 - \phi_s \right) / 2 \right] \times 100\% \tag{3}$$

126 The disease development was modelled by varying the stenosis size and incremental changes

127 in the spherical lipid pool volume. The lipid pool sphere was absent for the fully fibrous and

128 fully lipid plaque geometries. The fibrous cap was modelled as 0.25mm (Loree et al., 1992).

129 The geometry was meshed using hybrid and acoustic, linear, tetrahedron and hexahedron

130 elements. The ROI was meshed using an element edge length of 0.5mm. Propagating away

131 from the ROI the element edge length was gradually increased up to 2mm.

132 The blood was modelled as static and assigned acoustic properties (Hoskins, 2007). The soft

133 tissues were modelled as isotropic, Hookean, viscoelastic materials with a density of

134 1047kgm^{-3} (Hoskins, 2010) and a Poisson's ratio of 0.5 (Fung, 1993). The viscoelasticity was

135 represented by the dynamic shear modulus G; composed of the storage G' and loss modulus

136 G'' (Eq. 4). The dynamic modulus can be defined by the shear modulus μ, shear viscosity η

137 and frequency ω using a rheological model.

6

$$G(\omega) = G^{'}(\omega) + iG^{''}(\omega) \tag{4}$$

138   The viscoelastic properties of human arteries were taken from the most applicable research

139   available; these are summarised in Table 2. The material properties for the healthy and

140   diseased arterial wall, excluding the fibrous cap and lipid pool, were taken from the Neo-

141   Hookean hyperelastic model outlined by Holzapfel et al. (2002). This constitutive model

142   behaves like an elastic solid under small deformations (Bower, 2010). For these tissues the

143   viscoelasticity was modelled using the Voigt model (Eq. 5 - 7). The shear viscosity was fixed

144   at 80Pas (Valdez-Jasso et al., 2011).

$$G_{Voigt}(\omega) = \mu + i\omega\eta \tag{5}$$

$$G_{Voigt}{}^{'}(\omega) = \mu \tag{6}$$

$$G_{Voigt}{}^{''}(\omega) = \omega\eta \tag{7}$$

145   The surrounding tissue was given the viscoelastic properties of muscle (Klatt et al., 2010).

146   The values of the shear modulus and shear viscosity for the lipid pool and fibrous cap were

147   approximated by extrapolating the low frequency investigations of Loree et al. (1994), for a

148   0% cholesterol lipid, and Lee et al. (1991), for a cellular fibrous cap, into the frequency range

149   used in this study. The shear moduli of these extrapolated values are comparable to those

150   utilised by Holzapfel et al. (2002). The Maxwell model (Eq. 8 - 10) was used to represent the

151   viscoelastic behaviour of the surrounding tissue, fibrous cap and lipid pool, due to the

152   frequency dependence of the storage modulus demonstrated in the cited studies (Lee et al.,

153   1991; Loree et al., 1994; Klatt et al., 2010).

$$G_{Maxwell}(\omega) = \frac{i\omega\eta\mu}{\mu + i\omega\eta} \tag{8}$$

$$G_{Maxwell}{}^{'}(\omega) = \frac{\omega^2\eta^2\mu}{\mu^2 + \omega^2\eta^2} \tag{9}$$

$$G_{Maxwell}''(\omega) = \frac{\omega\eta\mu^2}{\mu^2 + \omega^2\eta^2} \tag{10}$$

154   Equations (11) and (12) define the Voigt and Maxwell model in terms of the loss angle, δ.

155   Under small oscillatory loads, the loss angle describes the response of a viscoelastic material.

156   The loss angle is defined as the arctangent of the loss to storage modulus (Fulcher et al.,

157   2009). When the stress and strain are in phase, the material response is purely elastic and the

158   loss angle is $0°$ (Barnes et al., 1989). When the stress and strain are out of phase, the material

159   response in purely viscous and the loss angle is $90°$ (Barnes et al., 1989).

$$\delta_{Voigt} = a\tan\frac{\omega\eta}{\mu} \tag{11}$$

$$\delta_{Maxwell} = a\tan\frac{\mu}{\omega\eta} \tag{12}$$

160   The Voigt model has shown a good correlation to in-vivo arterial pressure-area dynamics

161   (Valdez-Jasso et al., 2011). The storage modulus shows no dependence on excitation

162   frequency and the loss modulus increases with frequency. Hence the Voigt model

163   demonstrates an increasing loss angle with frequency, and the material response becomes

164   more viscous. The loss angle of the Maxwell model, as applied to the surrounding tissue,

165   lipid pool and fibrous cap, peaks at $\omega = \mu/\eta$. Above this frequency the decreasing loss

166   modulus dominates the loss angle and makes the tissue behave more elastically with

167   frequency.

168   The load nodes were isolated on the top surface of the model, shown in Fig. 1c. Harmonic,

169   shear wave excitation was simulated using a sinusoidal load of 6×10^{-4}N, applied parallel to

170   the Z axis. The excitation frequency was varied between 50Hz and 200Hz. Symmetric

171   boundary conditions were applied to the outer faces of the surrounding tissue, except the

172   loading surface.

2.2 Inversion Algorithm

173

174 The displacement was extracted using a pixel size of 1mm^2 through an imaging plane parallel

175 to the X and Y axes. The displacement was averaged over a 2mm slice thickness, centred on

176 the plaque, synonymous to an MRI voxel. Noise was added to the simulated data using the

177 method outlined by Miller et al. (2015). The standard deviation of the signal σ_{signal}, was

178 calculated using the real and imaginary wave amplitudes through the ROI. The distribution

179 was modelled as Gaussian with a zero mean and standard deviation, σ_{noise}, derived by (Eq.

180 13), where $1\% \le N \ge 20\%$.

$$\sigma_{noise} = N\% \cdot \sigma_{signal} \tag{13}$$

181 The displacement data was inverted into an elastogram using the Helmholtz algorithm (Eq.

182 14) (MATLAB R2011a, MathWorks, Natick, Massachusetts, USA). The derivation of this

183 algorithm is described by Klatt et al. (2006). The dynamic shear modulus $G(\omega)$, was yielded

184 by the Fourier transformed complex displacement U, wave excitation frequency ω and

185 tissue density ρ. The Laplacian, $\nabla^2 U$, was calculated from second order spatial derivatives

186 (Eq. 15). The dynamic shear modulus may be expressed in terms of the shear modulus μ and

187 shear viscosity η using a rheological model. In this study the Voigt model was utilised (Eq.

188 5).

$$G(\omega) = \frac{-\rho\omega^2 U}{\nabla^2 U} \tag{14}$$

$$\nabla^2 U = \frac{\partial^2 u}{\partial x^2} + \frac{\partial^2 u}{\partial y^2} \tag{15}$$

189 A 2D Butterworth filter was used to suppress noise and compression wave components (Klatt

190 et al., 2007; Clayton et al., 2011). The shear modulus formed the focus of this study; it is

191 displayed in elastograms and as a spatially averaged value through the ROI using the mean of

192 20 noisy cycles. Unless explicitly stated the technique parameters were fixed at $N = 2\%$,

193 100Hz with filter thresholds of 5m^{-1} and 1000000m^{-1}.

3. Results

195 The wave images of Fig. 2 show that as the composition of the plaque become more lipid, the

196 wave displacement through the low shear modulus material becomes visible. Although the

197 geometry of the lipid pools can-not be identified in the elastograms, the decrease in the shear

198 modulus can be seen through the stenosis as the lipid composition increases. The wave

199 images of Fig. 3 display decreasing wavelengths and increasing attenuation with increasing

200 frequency. The shear moduli through the elastograms increase with frequency. This

201 observation is complemented by Fig. 4c.

202 All data sets in Fig. 4 show a contrast between the fully fibrous and lipid compositions. The

203 magnitude of the mean shear modulus, the amount of contrast and the smoothness of the

204 trend is degraded by the increase in noise. Figure 4a shows that at $N = 2\%$, and a frequency

205 of 100Hz, there is a contrast between the incremental lipid volumes through all stenosis sizes.

206 At $N = 10\%$ and $N = 20\%$ the fully fibrous compositions maintain a higher mean shear

207 modulus than the fully lipid compositions, however the incremental decrease in contrast is

208 lost. Table 3 omits the effects of filters and displays the raw shear modulus variation with N

209 and plaque composition. Both Table 3 and Fig. 4a show degradation in contrast between

210 compositions with increasing noise. The predicted shear moduli are one or two orders of

211 magnitude lower than the simulated shear moduli.

212 Figure 4b shows that the 5m^{-1} to 1000000m^{-1} and 10m^{-1} to 1000m^{-1} filter ranges improve the

213 performance of the algorithm in terms of magnitudes and contrast between compositions. As

214 the filter thresholds are narrowed to between 15m^{-1} and 500m^{-1}, the distinctive wave

215 behaviour between compositions is over smoothed and the magnitudes and contrasts are

216 reduced. At the narrowest filter thresholds, similar to those found in experimental work (Klatt

217 et al., 2007), the algorithm becomes insensitive to any variation in noise.

218 **4. Discussion**

219 Harmonic wave propagation through an isotropic, homogeneous, incompressible, linear

220 elastic medium in the absence of body forces can be described by the Helmholtz equation

221 (Manduca et al., 2001). The limitations of the inversion algorithm are discussed in depth in

222 (Barbone and Gokhale, 2004; Papazoglou et al., 2008). In this study, the discrete and noisy

223 data through the heterogeneous application created artefacts, which can be seen in Fig. 2.

224 Through a homogeneous medium, harmonic wave propagation will lead to a displacement

225 and Laplacian term of opposite polarity. With reference to Eq. (14), this generates a positive

226 and thus real dynamic shear modulus. In discrete data the Laplacian is calculated from the

227 second order spatial gradients, Eq. (15), using two pixels adjacent to the pixel of interest.

228 Inhomogeneities through the medium, or step changes in the wave behaviour, change the

229 magnitude of this second order derivative. This can lead to errors in the shear moduli. This

230 exaggeration of gradients can be seen by comparing the visibly low level of noise in the wave

231 images of Fig 2. to the pronounced noise through the corresponding elastograms. Most

232 crucially, if the displacement and Laplacian are of the same polarity an impossible, negative

233 dynamic shear modulus is yielded. This numerical limitation was demonstrated by Thomas-

234 Seale (2015). In these cases the impossible values are equated to zero.

235 Along boundaries, similar artefacts can be identified as a line of over or underestimated

236 pixels. Beyond the X axis edge of the elastogram, there is no information. This reduces the

237 size of the Laplacian and creates an artefact of overestimated shear moduli. Since there is

238 minimal wave propagation parallel to the Y axis, there are no gradients and therefore no

239 artefacts adjacent to this edge. Along the edge of the lumen, there is an interface between the

240   blood and artery wall. Within 1mm there is also an interface between the artery wall and

241   surrounding tissue. On the upper interface there is an underestimated artefact of two pixels

242   deep. This is generated by the inflated spatial derivatives adjacent to the zero displacement of

243   the blood. On the lower interface there are lines of both underestimated pixels and

244   overestimated pixels. Observing the wave images of Fig. 2, the most pertinent difference

245   between the wave intersecting the upper and lower interface is the phase. Figure 3 shows that

246   the location of the zero pixel artefacts and the magnitude of the artefacts above and below the

247   lumen, change with frequency. It can be concluded that these artefacts show a dependency on

248   the phase of the wave. This reflection suggests that a multi-frequency inversion could

249   alleviate the effect of these artefacts.

250   Figure 3 and 4c show an increase in shear modulus with frequency. MRE excitation

251   frequency is strongly linked to resolution (Sinkus et al., 2000; Parker et al., 2005). The

252   increase in technique resolution with excitation frequency can be identified by the emerging

253   visibility of the lipid pool through the wave image at higher frequencies. As the wavelength

254   decreases, the contrast and detectability of inclusions are increased. Only a fraction of the

255   wave motion is captured within the plaque, therefore the algorithm can-not interpret the true

256   shear modulus. At 200Hz the wave propagation below the lumen is highly attenuated and the

257   amplitude oscillates around $\pm 5 \mu m$. This low amplitude combined with a 2mm element edge

258   and voxel of resolution 1mm^2 x 2mm generated a discretisation error which followed through

259   to errors in the shear moduli.

260   The degradation of the results of Table 3 and Fig. 4a with increasing noise stems from the

261   disruption in the clarity of the wave gradients and hence the ability of the algorithm to

262   calculate the shear modulus. Noise, increases step changes in the wave displacement and

263   hence exasperates the artefacts. This conclusion is supported by the increase in standard

264   deviation with noise, relative to the mean, for the majority of compositions in Table 3.

265 The Butterworth filter smooths out noise and compression wave components. Under pure

266 shear excitation, MRE through an incompressible medium allows compressional effects to be

267 neglected (Mariappan et al., 2010). In this simulated study the only interference with the

268 shear wave propagation are refracted and reflected waves, therefore noise was the dominant

269 component to be filtered.

270 The juxtaposition between the fact that filters smooth the data and therefore improve the

271 function of the inversion algorithm, and the fact the essence of this study lies in identifying

272 the difference in wave behaviour between the heterogeneous compositions, results in an

273 oxymoron. Thomas-Seale (2015) varied the thresholds through their full range and concluded

274 that over filtering of the wave images, through this heterogeneous application, can manipulate

275 the results. The filter thresholds could be optimised to this application and each frequency,

276 however even under these idealised conditions, the inversion algorithm is ill-suited to this

277 highly heterogeneous application. Attempting to improve its function by filtering also

278 smooths the essential contrast between compositions; this is shown in Fig. 4b.

279 The Helmholtz inversion algorithm has shown extreme sensitivity throughout this

280 application. The location, presentation and severity of artefacts have demonstrated a

281 dependence on noise, inhomogenieties and excitation frequency. This has created a level of

282 unpredictability in the analysis seen by the artefacts in the elastograms and sporadic high and

283 low values throughout the quantitative trends. In Fig. 4c, this is noticeable through the

284 200Hz, maximum noise analysis due to the combination of high noise and large gradients. In

285 conclusion, although this technique shows promise, identifying accurate mechanical

286 properties and contrast between plaque compositions hinges on developing a more applicable,

287 heterogeneous inversion algorithm.

288 This research, has allowed assessment of the technique and identification of the areas that

289 require development. However the idealised nature of the study is limiting. It has focussed on

290 a system with simplified parameters and has neglected the wave interaction with surrounding

291 organs and the cardiac cycle. The Voigt and Maxwell models are arguably not sophisticated

292 enough to fully describe the mechanical behaviour of arterial tissue and they are also not

293 ideal under wide frequency ranges (Yasar et al., 2013). The voxel resolution in this study was

294 idealised. Experimentally, an increase in resolution results in a decrease of signal to noise

295 ratio (McRobbie, 2007), therefore increasing the resolution will compound the limitations

296 seen in this research. This study has neglected the stiffness created by the shape of the ROI.

297 There is potential here to develop an inversion algorithm that is more applicable to the

298 cylindrical form of arterial structures. This concept has been broached in the work of

299 Kolipaka et al. (2009) through bounded media. Realistic methods of extracting and modelling

300 noise vary throughout MRE literature (Papazoglou et al., 2008; McGee et al., 2011). The

301 limitation of the method applied in this research (Miller et al., 2015), is that the standard

302 deviation, and hence noise level, changes with composition and frequency.

303 **5. Conclusion**

304 Simulated MRE through atherosclerotic plaques has allowed preliminary analysis of the

305 technique. A contrast between plaque composition and size was identified through the mean

306 shear modulus. However the inversion algorithm was sensitive to parameter variation and

307 constrained by the limitations of the discrete, noisy and heterogeneous data in this study.

308 Whilst filtering improved its accuracy, narrow filter thresholds also reduced the essential

309 contrast between the compositions. An increase in frequency, improved the resolution of the

310 technique in terms of magnitude and contrast. An inversion algorithm applicable to

311 heterogeneous tissue is required to continue this research.

312

313 **Acknowledgements**

315

316 Word Count: 3486

317

318 **Conflict of Interest Statement**

319 There are no personal or financial conflicts of interest associated with this study.

320

References

321 **References**

322 Ahmed, S. A., Giddens, D. P. 1983. Velocity-measurements in steady flow through
323   axisymmetric stenoses at moderate Reynolds-numbers. Journal of Biomechanics, 16,
324   505-516.

325 Baldewsing, R. A., De Korte, C. L., Schaar, J. A., Mastik, F., Van Der Steen, A. F. W. 2004.
326   Finite element modeling and intravascular ultrasound elastography of vulnerable
327   plaques: parameter variation. Ultrasonics, 42, 723-729.

328 Barbone, P. E., Gokhale, N. H. 2004. Elastic modulus imaging: on the uniqueness and
329   nonuniqueness of the elastography inverse problem in two dimensions. Inverse
330   Problems, 20, 283-296.

331 Barnes, H. A., Hutton, J. F., Walters, K. 1989. An Introduction to Rheology, Elsevier,
332   Oxford, UK.

333 Barrett, S. R. H., Sutcliffe, M. P. F., Howarth, S., Li, Z. Y., Gillard, J. H. 2009. Experimental
334   measurement of the mechanical properties of carotid atherothrombotic plaque fibrous
335   cap. Journal of Biomechanics, 42, 1650-1655.

336 Bertoglio, C., Barber, D., Gaddum, N., Valverde, I., Rutten, M., Beerbaum, P., Moireau, P.,
337   Hose, R., Gerbeau, J. F. 2014. Identification of artery wall stiffness: In vitro
338   validation and in vivo results of a data assimilation procedure applied to a 3D fluid-
339   structure interaction model. Journal of Biomechanics, 47, 1027-1034.

340 Bower, A. F. 2010. Applied Mechanics of Solids, CRC Press, Boca Raton, Florida.

341 Chen, Q. S., Ringleb, S. I., Manduca, A., Ehman, R. L., An, K. N. 2005. A finite element
342   model for analyzing shear wave propagation observed in magnetic resonance
343   elastography. Journal of Biomechanics, 38, 2198-2203.

344 Clayton, E. H., Garbow, J. R., Bayly, P. V. 2011. Frequency-dependent viscoelastic
345   parameters of mouse brain tissue estimated by MR elastography. Physics in Medicine
346   and Biology, 56, 2391-2406.

347 Corti, R., Fuster, V. 2011. Imaging of atherosclerosis: magnetic resonance imaging. European
348   Heart Journal, 32, 1709-1719.

349 Damughatla, A. R., Raterman, B., Sharkey-Toppen, T., Jin, N., Simonetti, O. P., White, R.
350   D., Kolipaka, A. 2015. Quantification of aortic stiffness using MR elastography and
351   its comparison to MRI-based pulse wave velocity. Journal of Magnetic Resonance
352   Imaging, 41, 44-51.

353 De Korte, C. L., Hansen, H. H. G., Van Der Steen, A. F. W. 2011. Vascular ultrasound for
354   atherosclerosis imaging. Interface Focus, 1, 565-575.

355   Doherty, J. R., Dumont, D. M., Trahey, G. E., Palmeri, M. L. 2013. Acoustic radiation force
356   impulse imaging of vulnerable plaques: a finite element method parametric analysis.
357   Journal of Biomechanics, 46, 83-90.

358   Falk, E., Shah, P. K., Fuster, V. 1995. Coronary plaque disruption. Circulation, 92, 657-671.

359   Franquet, A., Avril, S., Le Riche, R., Badel, P., Schneider, F. C., Boissier, C., Favre, J. P.
360   2013. Identification of the in vivo elastic properties of common carotid arteries from
361   MRI: A study on subjects with and without atherosclerosis. Journal of the Mechanical
362   Behavior of Biomedical Materials, 27, 184-203.

363   Fulcher, G. R., Hukins, D. W. L., Shepherd, D. E. T. 2009. Viscoelastic properties of bovine
364   articular cartilage attached to subchondral bone at high frequencies. BMC
365   Musculoskeletal Disorders, 10, 61.

366   Fung, Y. C. 1993. Biomechanics: Mechanical Properties of Living Tissues, Springer-Verlag,
367   New York.

368   Go, A. S., Mozaffarian, D., Roger, V. L., Benjamin, E. J., Berry, J. D., Blaha, M. J., Dai, S.
369   F., Ford, E. S., Fox, C. S., Franco, S., Fullerton, H. J., Gillespie, C., Hailpern, S. M.,
370   Heit, J. A., Howard, V. J., Huffman, M. D., Judd, S. E., Kissela, B. M., Kittner, S. J.,
371   Lackland, D. T., Lichtman, J. H., Lisabeth, L. D., Mackey, R. H., Magid, D. J.,
372   Marcus, G. M., Marelli, A., Matchar, D. B., Mcguire, D. K., Mohler, E. R., Moy, C.
373   S., Mussolino, M. E., Neumar, R. W., Nichol, G., Pandey, D. K., Paynter, N. P.,
374   Reeves, M. J., Sorlie, P. D., Stein, J., Towfighi, A., Turan, T. N., Virani, S. S., Wong,
375   N. D., Woo, D., Turner, M. B. 2014. Heart disease and stroke statistics - 2014 update.
376   A report from the American Heart Association. Circulation, 129, E28-E292.

377   Hamilton, P. K., Lockhart, C. J., Quinn, C. E., Mcveigh, G. E. 2007. Arterial stiffness:
378   clinical relevance, measurement and treatment. Clinical Science, 113, 157-170.

379   Holzapfel, G. A., Mulvihill, J. J., Cunnane, E. M., Walsh, M. T. 2014. Computational
380   approaches for analyzing the mechanics of atherosclerotic plaques: A review. Journal
381   of Biomechanics, 47, 859-869.

382   Holzapfel, G. A., Schulze-Bauer, C. a. J., Stadler, M. 2000. Mechanics of angioplasty: Wall,
383   balloon, and stent. In: Casey, J., Bao, G. (Eds.) Mechanics in Biology. The American
384   Society of Mechanical Engineers, New York.

385   Holzapfel, G. A., Sommer, G., Gasser, C. T., Regitnig, P. 2005. Determination of layer-
386   specific mechanical properties of human coronary arteries with nonatherosclerotic
387   intimal thickening and related constitutive modeling. American Journal of
388   Physiology-Heart and Circulatory Physiology, 289, H2048-H2058.

389   Holzapfel, G. A., Stadler, M., Schulze-Bauer, C. a. J. 2002. A layer-specific three-
390   dimensional model for the simulation of balloon angioplasty using magnetic

391   resonance imaging and mechanical testing. Annals of Biomedical Engineering, 30,
392   753-767.

393   Hoskins, P. R. 2007. Physical properties of tissues relevant to arterial ultrasound imaging and
394   blood velocity measurement. Ultrasound in Medicine and Biology, 33, 1527-1539.

395   Hoskins, P. R. 2010. Elastography. In: Hoskins, P. R., Martin, K., Thrush, A. (Eds.)
396   Diagnostic Ultrasound: Physics and Equipment. 2nd ed., Cambridge University Press,
397   Cambridge, UK.

398   Hoskins, P. R., Hardman, D. 2009. Three-dimensional imaging and computational modelling
399   for estimation of wall stresses in arteries. British Journal of Radiology, 82, S3-S17.

400   Kenyhercz, W. E., Raterman, B., Illapani, V. S. P., Dowell, J., Mo, X., White, R. D.,
401   Kolipaka, A. 2015. Quantification of aortic stiffness using magnetic resonance
402   elastography: measurement reproducibility, pulse wave velocity comparison, changes
403   over cardiac cycle, and relationship with age. Magnetic Resonance in Medicine, (In
404   Print).

405   Klatt, D., Asbach, P., Rump, J., Papazoglou, S., Somasundaram, R., Modrow, J., Braun, J.,
406   Sack, I. 2006. In vivo determination of hepatic stiffness using steady-state free
407   precession magnetic resonance elastography. Investigative Radiology, 41, 841-848.

408   Klatt, D., Hamhaber, U., Asbach, P., Braun, J., Sack, I. 2007. Noninvasive assessment of the
409   rheological behavior of human organs using multifrequency MR elastography: a study
410   of brain and liver viscoelasticity. Physics in Medicine and Biology, 52, 7281-7294.

411   Klatt, D., Papazoglou, S., Braun, J., Sack, I. 2010. Viscoelasticity-based MR elastography of
412   skeletal muscle. Physics in Medicine and Biology, 55, 6445-6459.

413   Kolipaka, A., Mcgee, K. P., Manduca, A., Romano, A. J., Glaser, K. J., Araoz, P. A., Ehman,
414   R. L. 2009. Magnetic resonance elastography: inversions in bounded media. Magnetic
415   Resonance in Medicine, 62, 1533-1542.

416   Kolipaka, A., Woodrum, D., Araoz, P. A., Ehman, R. L. 2012. MR elastography of the in
417   vivo abdominal aorta: A feasibility study for comparing aortic stiffness between
418   hypertensives and normotensives. Journal of Magnetic Resonance Imaging, 35, 582-
419   586.

420   Lee, R. T., Grodzinsky, A. J., Frank, E. H., Kamm, R. D., Schoen, F. J. 1991. Structure-
421   dependent dynamic mechanical behaviour of fibrous caps from human atherosclerotic
422   plaques. Circulation, 83, 1764-1770.

423   Libby, P., Ridker, P. M., Maseri, A. 2002. Inflammation and atherosclerosis. Circulation,
424   105, 1135-1143.

425 Loree, H. M., Kamm, R. D., Stringfellow, R. G., Lee, R. T. 1992. Effects of fibrous cap
426   thickness on peak circumferential stress in model atherosclerotic vessels. Circulation
427   Research, 71, 850-858.

428 Loree, H. M., Tobias, B. J., Gibson, L. J., Kamm, R. D., Small, D. M., Lee, R. T. 1994.
429   Mechanical properties of model atherosclerotic lesion lipid pools. Arteriosclerosis and
430   Thrombosis, 14, 230-234.

431 Manduca, A., Oliphant, T. E., Dresner, M. A., Mahowald, J. L., Kruse, S. A., Amromin, E.,
432   Felmlee, J. P., Greenleaf, J. F., Ehman, R. L. 2001. Magnetic resonance elastography:
433   Non-invasive mapping of tissue elasticity. Medical Image Analysis, 5, 237-254.

434 Mariappan, Y. K., Glaser, K. J., Ehman, R. L. 2010. Magnetic resonance elastography: a
435   review. Clinical Anatomy, 23, 497-511.

436 Mcgee, K. P., Lake, D., Mariappan, Y., Hubmayr, R. D., Manduca, A., Ansell, K., Ehman, R.
437   L. 2011. Calculation of shear stiffness in noise dominated magnetic resonance
438   elastography data based on principal frequency estimation. Physics in Medicine and
439   Biology, 56, 4291-4309.

440 Mcrobbie, D. W. 2007. MRI from Picture to Proton, Cambridge University Press,
441   Cambridge, UK.

442 Mendis, S., Puska, P., Norrving, B. 2011. Global Atlas on Cardiovascular Disease and
443   Control, World Health Organisation, Geneva.

444 Miller, R., Jiang, H., Mazumder, R., Cowan, B., Nash, M., Kolipaka, A., Young, A.
445   Determining anisotropic myocardial stiffness from magnetic resonance elastography:
446   a simulation study. In: Functional Imaging and Modelling of the Heart: 8th
447   International Conference, FIMH 2015, June 25-17, 2015, The Netherlands: Springer,
448   346-354.

449 Mulder, W. J. M., Jaffer, F. A., Fayad, Z. A., Nahrendorf, M. 2014. Imaging and
450   nanomedicine in inflammatory atherosclerosis. Science Translational Medicine, 6, 1-
451   11.

452 Muthupillai, R., Lomas, D. J., Rossman, P. J., Greenleaf, J. F., Manduca, A., Ehman, R. L.
453   1995. Magnetic-resonance elastography by direct visualization of propagating
454   acoustic strain waves. Science, 269, 1854-1857.

455 Packard, R. R. S., Libby, P. 2008. Inflammation in atherosclerosis: From vascular biology to
456   biomarker discovery and risk prediction. Clinical Chemistry, 54, 24-38.

457 Papazoglou, S., Hamhaber, U., Braun, J., Sack, I. 2008. Algebraic Helmholtz inversion in
458   planar magnetic resonance elastography. Physics in Medicine and Biology, 53, 3147-
459   3158.

460   Parker, K. H. 2009. A brief history of arterial wave mechanics. Medical & Biological
461   Engineering & Computing, 47, 111-118.

462   Parker, K. J., Taylor, L. S., Gracewski, S., Rubens, D. J. 2005. A unified view of imaging the
463   elastic properties of tissue. Journal of the Acoustical Society of America, 117, 2705-
464   2712.

465   Rothwell, P. M., Gutnikov, S. A., Warlow, C. P., European Carotid Surgery, T. 2003.
466   Reanalysis of the final results of the European Carotid Surgery Trial. Stroke, 34, 514-
467   523.

468   Sarvazyan, A., Hall, T. J., Urban, M. W., Fatemi, M., Aglyamov, S. R., Garra, B. S. 2011. An
469   overview of elastography - an emerging branch of medical imaging. Current Medical
470   Imaging Reviews, 7, 255-282.

471   Sinkus, R., Lorenzen, J., Schrader, D., Lorenzen, M., Dargatz, M., Holz, D. 2000. High-
472   resolution tensor MR elastography for breast tumour detection. Physics in Medicine
473   and Biology, 45, 1649-1664.

474   Tang, D. L., Yang, C., Kobayashi, S., Ku, D. N. 2004. Effect of a lipid pool on stress/strain
475   distributions in stenotic arteries: 3-D fluid-structure interactions (FSI) models. Journal
476   of Biomechanical Engineering - Transactions of the ASME, 126, 363-370.

477   Thomas-Seale, L. E. J. 2015. The Application of Magnetic Resonance Elastography to
478   Atherosclerosis. Doctor of Philosophy, Thesis, The University of Edinburgh.

479   Thomas-Seale, L. E. J., Klatt, D., Pankaj, P., Roberts, N., Sack, I., Hoskins, P. R. 2011. A
480   simulation of the magnetic resonance elastography steady state wave response
481   through idealised atherosclerotic plaques. IAENG International Journal of Computer
482   Science, 38, 394-400.

483   Townsend, N., Wickramasinghe, K., Bhatnagar, P., Smolina, K., Nichols, M., Leal, J.,
484   Luengo-Fernandez, R., Rayner, M. 2012. Coronary heart disease statistics 2012
485   edition, British Heart Foundation, London, UK.

486   Valdez-Jasso, D., Bia, D., Zocalo, Y., Armentano, R. L., Haider, M. A., Olufsen, M. S. 2011.
487   Linear and nonlinear viscoelastic modeling of aorta and carotid pressure-area
488   dynamics under in Vivo and ex vivo conditions. Annals of Biomedical Engineering,
489   39, 1438-1456.

490   Van Houten, E. E. W., Miga, M. I., Weaver, J. B., Kennedy, F. E., Paulsen, K. D. 2001.
491   Three-dimensional subzone-based reconstruction algorithm for MR elastography.
492   Magnetic Resonance in Medicine, 45, 827-837.

493   Vanepps, J. S., Vorp, D. A. 2007. Mechanopathobiology of atherogenesis: A review. Journal
494   of Surgical Research, 142, 202-217.

495 Woodrum, D. A., Herrmann, J., Lerman, A., Romano, A. J., Lerman, L. O., Ehman, R. L.
496   2009. Phase-contrast MRI-based elastography technique detects early hypertensive
497   changes in ex vivo porcine aortic wall. Journal of Magnetic Resonance Imaging, 29,
498   583-587.

499 Woodrum, D. A., Romano, A. J., Lerman, A., Pandya, U. H., Brosh, D., Rossman, P. J.,
500   Lerman, L. O., Ehman, R. L. 2006. Vascular wall elasticity measurement by magnetic
501   resonance imaging. Magnetic Resonance in Medicine, 56, 593-600.

502 Xu, L., Chen, J., Glaser, K. J., Yin, M., Rossman, P. J., Ehman, R. L. 2013. MR elastography
503   of the human abdominal aorta: A preliminary study. Journal of Magnetic Resonance
504   Imaging, 38, 1549-1553.

505 Xu, L., Chen, J., Yin, M., Glaser, K. J., Chen, Q. S., Woodrum, D. A., Ehman, R. L. 2012.
506   Assessment of stiffness changes in the ex vivo porcine aortic wall using magnetic
507   resonance elastography. Magnetic Resonance Imaging, 30, 122-127.

508 Yasar, T. K., Royston, T. J., Magin, R. L. 2013. Wideband MR elastography for
509   viscoelasticity model identification. Magnetic Resonance in Medicine, 70, 479-489.

510 Zhang, N., Chen, J., Yin, M., Glaser, K. J., Xu, L., Ehman, R. L. 2016. Quantification of
511   regional aortic stiffness using MR elastography: A phantom and ex-vivo porcine aorta
512   study. Magnetic Resonance Imaging, 34, 91-96.

513 Zheng, Y., Chan, Q. C. C., Li, G., Lam, E. Y., Yang, E. S. 2007. A study of femoral artery by
514   twin drivers in magnetic resonance interference elastography. In: The 29th Annual
515   International Conference of the IEEE Engineering in Medicine and Biology Society,
516   Aug 22-26, 2007, Lyon, France, 2034-2037.

517

518

529

530

545

546

Figure 1 Rev. 2
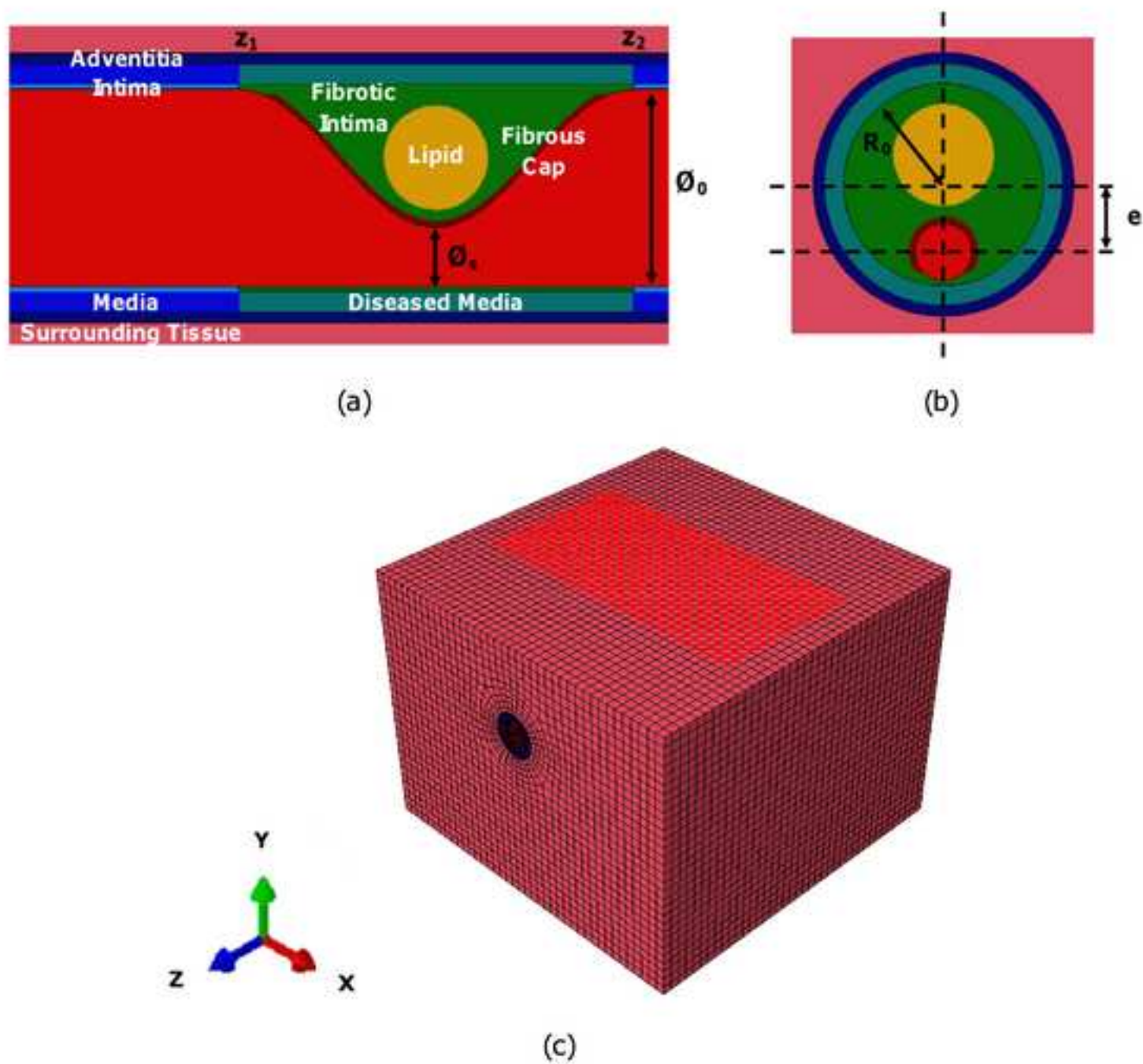**Click here to download high resolution image**
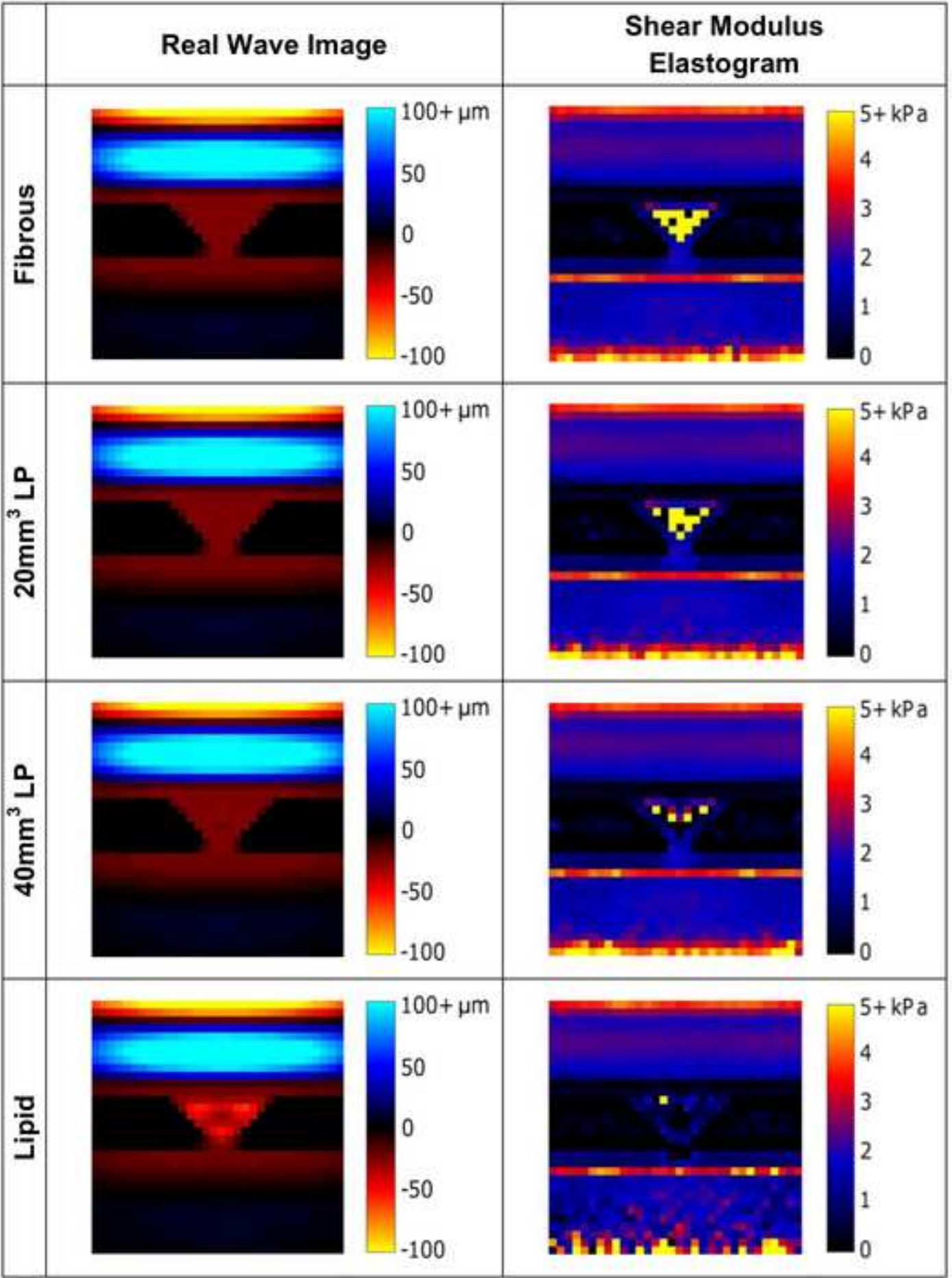
(a)

(b)

(c)

Figure 2 Rev. 2
Click here to download high resolution image

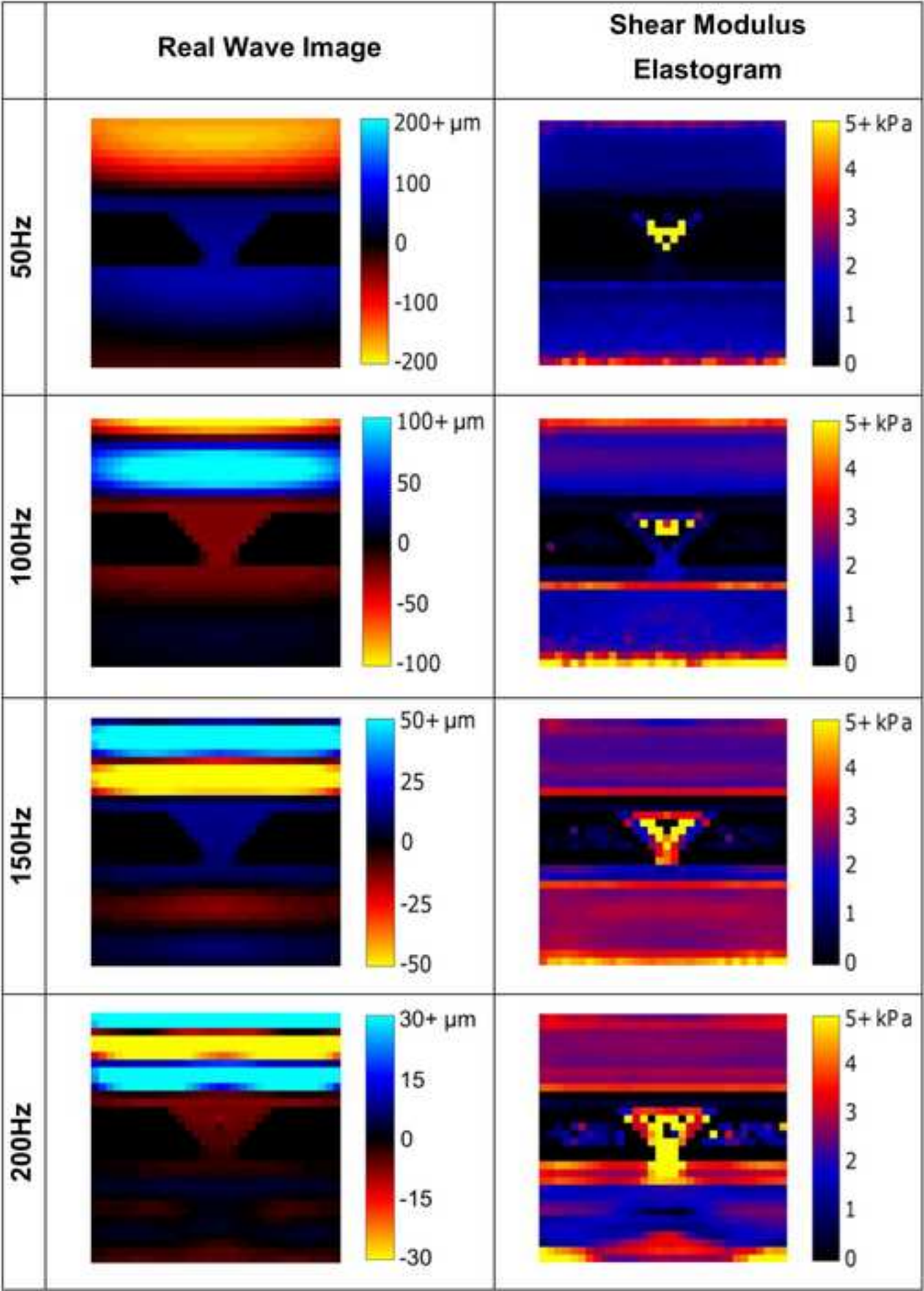**Figure 3 Rev. 2**
Click here to download high resolution image
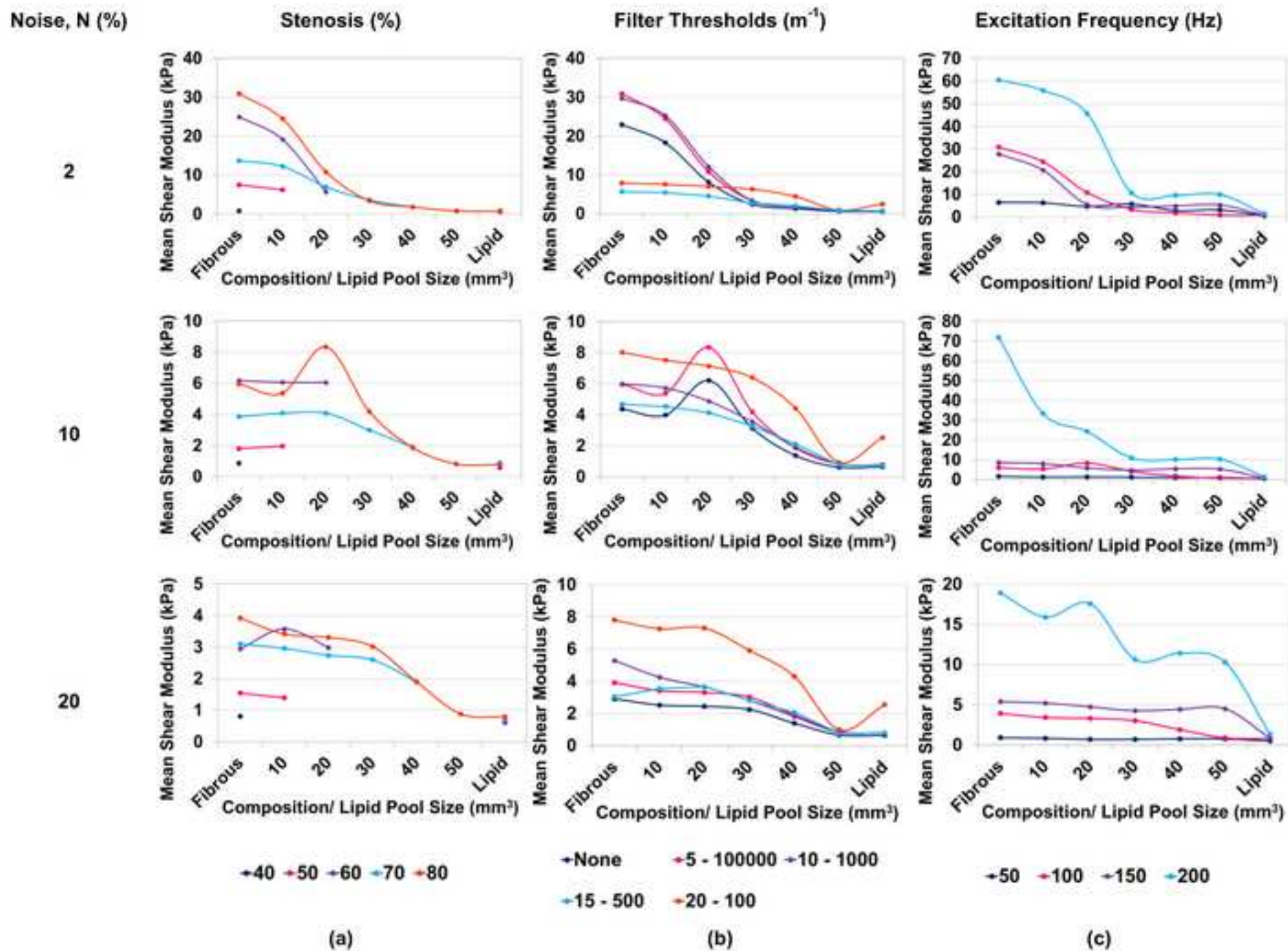
Table 1 Rev. 2

Tissue	Geometric Parameter	Value
Surrounding Tissue	Length	80.00 mm
	Width	80.00 mm
	Depth	60.00 mm
Stenosis	Length	14.52 mm
Intima	Inner Radius	3.63 mm*
	Thickness	0.17 mm*
Media	Inner Radius	3.80 mm*
	Thickness	0.73 mm*
Adventitia	Inner Radius	4.53 mm*
	Thickness	0.43 mm*
Fibrous Cap	Thickness	0.25/0.5/0.75mm**
Lipid Pool	Volume	0/10/20/30/40/50/ Total mm^3

Table 2 Rev. 2

Tissue	Density (kgm^{-3})	Shear Modulus (kPa)	Bulk Modulus (kPa)	Shear Viscosity (Pas)
Surrounding Tissue	1047*	2.3**	-	17.0**
Intima	1047*	150.0[+]	-	80.0[++]
Fibrotic Intima	1047*	221.0[+]	-	80.0[++]
Media	1047*	34.0[+]	-	80.0[++]
Diseased Media	1047*	757.0[+]	-	80.0[++]
Adventitia	1047*	50.0[+]	-	80.0[++]
Fibrous Cap	1047*	208.4[#]	-	19820.0[#]
Lipid	1047*	0.1[##]	-	6.4[##]
Blood	1060[^]	-	2.67x10^{6}[^]	-

Table 3 Rev. 2

Noise, N (%)	Mean/Standard Deviation Predicted Shear Modulus (kPa)						
	Fibrous Plaque	Lipid Pool Volume					Lipid Plaque
		10mm³	20mm³	30mm³	40mm³	50mm³	
Omitted	30.9	29.9	5.2	2.4	1.3	0.6	0.6
1	30.1/5.0	22.5/2.4	9.0/4.5	2.4/0.1	1.3/0.0	0.6/0.0	0.6/0.0
2	23.0/4.3	18.3/3.7	8.2/3.4	2.4/0.2	1.3/0.0	0.6/0.0	0.6/0.0
5	7.3/2.3	9.6/5.7	5.8/2.6	3.0/1.2	1.3/0.0	0.6/0.0	0.6/0.0
10	4.4/0.8	4.0/0.8	6.2/5.3	3.1/1.6	1.4/0.1	0.6/0.0	0.6/0.1
15	3.2/1.1	3.7/1.1	3.1/1.6	2.1/0.4	1.4/0.3	0.6/0.1	0.7/0.2
20	2.9/1.0	2.5/0.7	2.4/0.7	2.2/0.6	1.4/0.2	0.7/0.1	0.6/0.1
Mean Simulated Shear Modulus	**219.6**	**190.2**	**172.9**	**158.5**	**145.5**	**133.6**	**23.1**

Conflict of Interest Statement

There are no personal or financial conflicts of interest associated with this study.